PHYSICAL REVIEW B, VOLUME 63, 205117

Local symmetry and bonding effects on electron energy-loss near-edge structures: *Ab initio* study of an NiAl grain boundary

D. A. Pankhurst*
Department of Materials Science and Metallurgy, University of Cambridge, Pembroke Street, Cambridge, CB2 3QZ, United Kingdom

G. A. Botton
Materials Technology Laboratory, Natural Resources Canada, 568 Booth Street, Ottawa, K1A 0G1, Canada

C. J. Humphreys
Department of Materials Science and Metallurgy, University of Cambridge, Pembroke Street, Cambridge, CB2 3QZ, United Kingdom

(Received 23 October 2000; revised manuscript received 13 February 2001; published 8 May 2001)

Electron energy-loss near-edge structure (ELNES) reflects an unoccupied, site-, and angular-momentum-projected density-of-states. Using a focused electron probe, one can measure the local electronic structure at atomic spatial resolution at defects such as grain boundaries. We have calculated partial densities of *d* states and L_3 ELNES of Ni atoms at a $\Sigma 3$ (111) grain boundary in B2 NiAl using the full-potential linearized augmented plane-wave method, carrying out *ab initio* structural relaxations. We observe large changes in the partial density of *d* states for Ni atoms near the boundary, which can be related to broken symmetry and reduced cohesion. These changes manifest themselves also in the Ni L_3 ELNES, which measures the unoccupied density of Ni *d* states. The characteristic signal should be measurable experimentally at atomic spatial resolution on a spherical-aberration-corrected scanning transmission electron microscope. A spatially averaged interfacial signal should be measurable using a larger probe on a conventional instrument. The importance of carrying out electronic structure calculations in order to understand ELNES from grain boundaries is emphasized.

DOI: 10.1103/PhysRevB.63.205117 PACS number(s): 73.20.−r, 79.20.−m, 61.72.Mm, 71.20.Lp

I. INTRODUCTION

Electron energy-loss spectrometry (EELS) in the electron microscope is a powerful tool with which to probe the local electronic structure of solids. The energy-loss near-edge structure (ELNES) observed after the onset of a core-level ionization edge reflects a local, weighted density of final states to which core electrons are excited by fast incident electrons. Therefore ELNES is highly sensitive to the symmetry of the local chemical environment of the excited atoms. Furthermore, by focusing the incident beam to a fine probe, it is possible to obtain spectra that reveal atomic-scale variations in the electronic structure at interfaces and dislocations.[1–3]

The purpose of this paper is to predict and understand the changes in the ELNES that might be seen in atomic-column-resolved Ni L_3 spectra from clean grain boundaries in the *B*2 intermetallic NiAl. Grain boundaries in NiAl, as in many materials, play a crucial role in determining its mechanical properties, which have been the subject of much research over the past few decades.[4,5] This effort has been driven largely by the need for new high-temperature materials for gas turbine blades.[6] A significant part of this effort has been directed towards understanding the bonding mechanism in NiAl and how this relates to its brittleness at room temperature. To this end the electronic structure of NiAl has been investigated extensively using a variety of experimental and modeling techniques: x-ray emission spectroscopy,[7–9] x-ray photoelectron and Bremsstrahlung isochromat spectroscopy,[10–15] x-ray absorption spectroscopy (XAS),[16,17] EELS,[18,19] density-functional theory (DFT),[18–30] and tight-binding theory.[31–34]

Apart from its potential technological benefits, NiAl is an apt choice for this paper for other reasons: First, the close correspondence between experimental Ni L_3 spectra and those calculated from one-electron band theory indicates that many-body effects, which in general complicate the interpretation of ELNES, are not important in this case. It can further be shown that the Ni L_3 ELNES in NiAl approximates an unoccupied, single-particle Ni *d* density-of-states (DOS).[18,19] Therefore the DFT-based full-potential linearized augmented plane-wave (FLAPW) method used in this paper should be adequate to describe all of the features of the experimental spectra. Second, there is an intimate relationship between the Ni L_3 ELNES and the bonding in NiAl. Most authors have concluded that the dominant contribution to the cohesive energy of this compound comes from hybridization of localized, directional Ni *d* states with more diffuse, nearly free-electronlike Al *sp* states. This simple concept, although inadequate to explain the detailed fine structure of the DOS resulting from a complex mixing of *s*, *p*, and *d* (and in principle greater *l*) symmetries, does explain its basic topology. The DOS (see Fig. 1), which is dominated by *d* symmetries, is split by the *sp*-*d* hybridization into a bonding-antibonding complex separated by weakly interacting ‘‘nonbonding’’ states of a different angular symmetry (see Sec. V A for a detailed description).[35] In between these are regions of low DOS, often referred to as ‘‘pseudogaps.’’[31,33] ELNES measures an unoccupied DOS, so given that the Fermi level lies in the nonbonding region, a two-peak structure is observed in the unoccupied Ni *d* DOS and hence in the Ni $L_{2,3}$ ELNES. Thus the ELNES measures a region of the DOS that will be highly sensitive to changes in the local symmetry and bond-

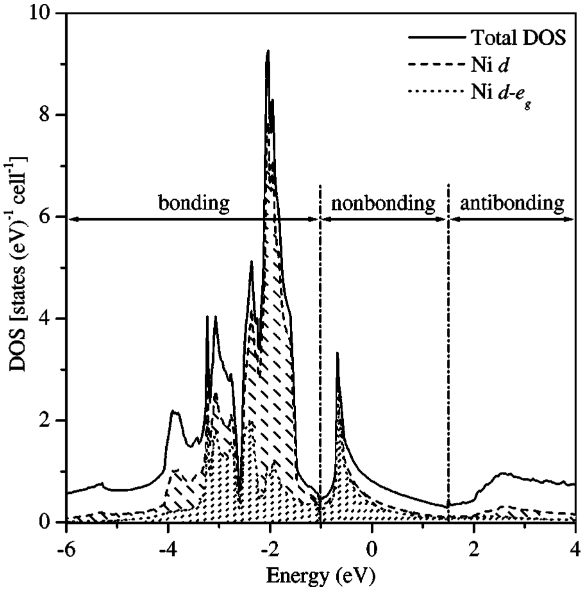

FIG. 1. Total and Ni d density of states calculated for bulk NiAl; the areas of the shaded regions correspond to the contribution of the e_g and t_{2g} components to the d DOS (i.e., $d=t_{2g}+e_g$). $E_F=0$. Bonding, nonbonding, and antibonding regions are labeled.

ing at grain boundaries, where substantial relaxations and atomic rearrangements occur.

The grain boundary studied here is based on the $\Sigma 3$ (111) twin, which has $\overline{6}2m$ point symmetry at the site of an atom in the boundary plane. Nadarzinsky and Ernst investigated this structure experimentally using high-resolution electron microscopy,[36] and Hagen and Finnis carried out an atomistic simulation.[37] They concluded that (i) the boundary plane is occupied by Al atoms, and (ii) there is a measurable expansion perpendicular to the boundary plane. The structural relaxations are due to a strong repulsive force between Ni atoms either side of the grain boundary plane.

We present partial DOS and Ni L_3 ELNES associated with changes in the electronic structure at the $\Sigma 3$ (111) grain boundary in NiAl, calculated after a full *ab initio* minimization of the atomic forces normal to the boundary plane. We carried out the calculations using the WIEN97 FLAPW code.[38] We observe large changes in the local electronic structure at the grain boundary, similar to those we observed in preliminary studies.[39,40] We predict that corresponding changes in the Ni L_3 ELNES should be measurable experimentally at grain boundaries using a focused probe.

II. THEORY

A. ELNES in the single-particle approximation

The inelastic scattering of fast electrons by atoms is described quantum mechanically by the Bethe theory.[41,42] In the first Born approximation the double differential cross section for the scattering of an incident electron with wave vector $\mathbf{k}_0$ into a state with final wave vector $\mathbf{k}$, through solid angle Ω, transferring energy E and momentum $\hbar(\mathbf{k}_0-\mathbf{k})=\hbar\mathbf{q}$ to the target atom is

$$\frac{\partial^2\sigma}{\partial E\,\partial\Omega}=\frac{4\gamma^2}{a_0^2q^4}\frac{k}{k_0}S(\mathbf{q},E), \tag{1}$$

where $\gamma=\sqrt{1-v^2/c^2}$ is the relativistic Lorentz factor and a_0 the Bohr radius. $S(\mathbf{q},E)$ is the dynamic form factor (DFF), for which the single-particle expression is

$$S(\mathbf{q},E)=\sum_{i,f}|\langle i|e^{i\mathbf{q}\cdot\mathbf{r}}|f\rangle|^2\delta(E+E_i-E_f), \tag{2}$$

where the sum is over all initial and final one-electron states $(i,\ f)$.

In the limit of small momentum transfer $(e^{i\mathbf{q}\cdot\mathbf{r}}\approx 1+i\mathbf{q}\cdot\mathbf{r})$, the DFF reduces further to the dipole-approximated form,

$$\tilde{S}(\hat{\mathbf{q}},E)=\frac{S}{q^2}\approx\sum_{i,f}|\hat{\mathbf{q}}.\langle i|\mathbf{r}|f\rangle|^2\delta(E+E_i-E_f), \tag{3}$$

where $\hat{\mathbf{q}}$ is a unit vector in the direction of $\mathbf{q}$. This expression is essentially the same as that which appears in the cross sections for x-ray emission and absorption, which can be obtained by replacing $\hat{\mathbf{q}}$ with $\hat{\mathbf{e}}$, the polarization vector of an emitted or absorbed photon.[43,44] Hence, in this limit, ELNES and x-ray absorption near-edge structures (XANES) are equivalent.

The $\langle i|$ terms in the matrix elements of Eq. (2, 3) weight the DFF strongly in the core region, where the effective potential felt by the final state $|f\rangle$ is roughly spherical. Therefore, a basis of angular momentum eigenfunctions is well-suited to the expansion of the final-state wave function in this region. Using such a basis, the matrix elements are separable into radial and angular parts, and upon averaging over all directions of $\hat{\mathbf{q}}$ (or $\hat{\mathbf{e}}$), the DFF factorizes into a sum over atomic matrix elements multiplied by local, angular momentum selected, single-particle densities-of-states. This factorization has been obtained rigorously for Slater's augmented plane-wave basis[45] with application to x-ray emission,[46,47] XANES,[44] and recently as a special case for orientation dependent ELNES.[48,49]

The FLAPW basis does not strictly fulfill the DFF separability criterion because it has a more flexible basis set that is apt to describe nonspherical (muffin tin) MT wave functions and potentials. However, for deep core edges such as Ni $L_{2,3}$ the core states $(2p_{1/2},2p_{3/2})$ are well localized. Only where there is a significant overlap between the core and final state is there a significant contribution to the DFF. Since the Ni $2p_{3/2}$ wave function has 99% of its weight within a radius of 0.62 atomic units (a.u.) from the nucleus—a region where the potential is approximately spherical—the factorization still holds to a good approximation for the Ni L_3 edge. Therefore it is justifiable to calculate the absorption edges using the spherical parts of the FLAPW basis functions and potential inside the MT spheres.

In the small-$\mathbf{q}$ limit, dipole selection rules dictate which transitions are allowed $(\Delta l=\pm 1)$ and the matrix elements become independent of $\mathbf{q}$. The dipole-approximated DFF for transitions from a core state $|\phi_{lj}\rangle$ with orbital (total) angular momentum quantum number l (j) can thus be written as[44]

$$\tilde{S}_{lj}(E)=\sum_{l'} W_{l,l'}\frac{|\langle \phi_{lj}|r|u_{l'}(E)\rangle|^2}{\langle u_{l'}(E)|u_{l'}(E)\rangle}N_{l'}(E), \tag{4}$$

where the weighting factor $W_{l,l'}$, is nonzero only when $l'=l\pm1$,

$$W_{l,l'}=\frac{1}{3}\,\frac{2j+1}{2(2l+1)}\left(\frac{l}{2l-1}\,\delta_{l-1,l'}+\frac{l+1}{2l+3}\,\delta_{l+1,l'}\right). \tag{5}$$

The bra-ket combinations in Eq. (4) denote integrals within a single MT sphere, where $u_{l'}(E)$ are the l' components of the radial conduction band wave function. $N_{l'}$ is the unoccupied l'- and MT-projected DOS. It follows from Eqs. (4) and (5) that the Ni $L_{2,3}$ ELNES is roughly proportional to a local density of Ni d states because:[19,44] (i) the overall DOS is dominated by d symmetries, (ii) the matrix elements [second term on the right-hand side of Eq. (4)] are slowly varying functions of energy, and (iii) the matrix element for $2p\rightarrow s$ transitions is relatively small because of cancellations in the radial integral.

While the dipole approximation does certainly not apply to the whole EEL spectrum, it is usually good enough to describe the region close to the onset of a given edge where $\Delta l=\pm1$ transitions dominate over a broad range of $\mathbf{q}$.[42,50] The small-$\mathbf{q}$ regime can be enforced experimentally by using apertures to limit the range of collected scattering angles. However, the factorization of the DFF only holds if all directions of $\hat{\mathbf{q}}$ are sampled. If there is anisotropy in the electronic structure—this is quite likely at a grain boundary—care must be exercised in setting up the scattering geometry so as to give the different $\hat{\mathbf{q}}$'s their proper weighting.[51]

B. Limitations of the single-particle approximation

In the strictest sense, the Kohn-Sham eigenvalues and wave functions are only meaningful in describing ground-state properties (charge density, total energy), and there is no formal justification for interpreting unoccupied energy eigenvalues as an excitation spectrum.[52] First of all, the unoccupied Kohn-Sham orbitals are calculated in the ground-state potential due to all of the other electrons and nuclei, so the effect of any relaxation of the one-electron states, due to the creation of the core hole, is ignored. The ‘‘core-hole effect’’ is often characterized by a narrowing of the spectral features in the ELNES and a buildup of intensity near the edge threshold compared with the ground-state, single-particle DOS.[53,54] No features of this type have been observed in the Ni $L_{2,3}$ edges of Ni-Al alloys and the agreement between experimental and DFT-calculated spectra is excellent,[18,19] which suggests that the perturbations caused by the $2p_{1/2,3/2}$ core holes are negligible.

Stern and Rehr discussed the validity of the single-particle approximation for transition metal $L_{2,3}$ spectra using a modified Hartree-Fock approach.[55] Imposing the requirement that the excited electron be orthogonal to all *initially* occupied one-electron states and that the core hole be orthogonal to all *finally* occupied states, they predicted two limiting cases for which the single-particle approximation is valid: (i) The ground-state potential and single-particle DOS are appropriate when the ejected core electron fills the d shell. (ii) The single-particle potential and DOS of an excited atom is appropriate when the core electron is excited to an empty d shell. The Ni d-band is nearly full in the Ni-Al alloys, and thus falls roughly into the first category, hence the good agreement between the experimental and ground-state, single-particle calculations. However, as Stern and Rehr pointed out, in general the excitation process is a many-body problem that is described inadequately in the single-particle approximation.

Another point concerns inadequate treatment of exchange and correlation in the excited states. The various approximations to exchange and correlation used commonly in DFT treat the exchange-correlation potential V_{xc}, as a function of local variables (e.g., the local charge density), but as a constant of energy. Formal many-body theory predicts a pronounced state dependence of exchange and correlation contributions to the quasiparticle energy through a nonlocal (and generally complex) self-energy operator $\Sigma(\mathbf{r},\mathbf{r}';E)$,[56] to which V_{xc} is a reasonable approximation in the ground state, but generally a poor one for excited states. The most severe consequences are observed for semiconductors and insulators, whose band gaps are underestimated grossly in DFT calculations.[57] Simple metals do not present such a problem because of effective screening, which keeps the self-energy roughly constant up to about 10 eV above the Fermi energy.[58] At higher excitation energies, V_{xc} tends to overestimate the exchange-correlation interactions because the ejected electrons, having greater kinetic energy, are less effectively screened. This leads to a discrepancy between experimentally-measured and DFT-calculated DOS that increases with excitation energy.[59] This is to be distinguished from any effects due to the core hole, which can be treated as a separate quasiparticle.

The experimentally measured quasiparticle excitations have finite lifetimes, which result in broadening of the spectral features. This information is contained in the imaginary part of the self-energy, $\mathrm{Im}[\Sigma(\mathbf{r},\mathbf{r}';E)]$, but the DFT eigenvalues are real and so do not carry this information. Assuming that the features of the DFT-calculated ELNES in the region of interest are essentially faithful to the quasiparticle energies, the finite lifetimes of the core hole and the secondary electron can be accounted for phenomenologically by applying an energy-dependent Lorentzian smoothing to the calculated spectrum.[44]

NiAl is a good, weakly correlated metal that shows no measurable magnetic ordering down to temperatures of a few Kelvin.[60,61] Therefore, according to the above arguments, the single-particle DOS and matrix elements calculated using the local-density approximation (LDA) within DFT (up to 10 eV above the Fermi energy) should be adequate to describe the effects we might see in experimental Ni $L_{2,3}$ spectra from grain boundaries in NiAl.

C. Charge-density maps

One if the main outputs of density functional calculations is the self consistent charge density, given by the sum over all one-electron probability amplitudes (the moduli squared of the Kohn-Sham orbitals):

$$\rho^{scf}(\mathbf{r})=\sum_i |\psi_{\mathbf{k}}^i(\mathbf{r})|^2. \tag{6}$$

This expression, which neglects electron spin, gives the correct total charge density when evaluated within an energy window from $-\infty$ to E_F, but it is often useful to evaluate it in some other energy window corresponding to a particular region of the DOS. This window need not be solely in the occupied region of the DOS: The ''unoccupied'' charge density evaluated in a window above E_F represents a real-space distribution of excitation probabilities. These concepts will provide a real-space picture to aid in the interpretation of the calculated DOS and ELNES.

Another useful quantity is the difference (or bonding) charge density. It is a measure of the charge relaxation that occurs on forming the solid from isolated atoms, and is defined as the self-consistent ground-state charge density of the solid minus a linear superposition of free-atom charge densities centered on the atomic coordinates $\{\mathbf{R}_i\}$ of the solid:

$$\rho^{diff}(\mathbf{r})=\rho^{scf}(\mathbf{r})-\sum_i \rho_i^{at}(\mathbf{r}-\mathbf{R}_i). \tag{7}$$

III. COMPUTATIONAL DETAILS

We performed all of the calculations presented below using the WIEN97 FLAPW code.[38,62] All band calculations were non-spin-polarized, and used the LDA to the exchange-correlation functional as parametrized by Perdew and Wang.[63] We treated core states fully relativistically but included only scalar-relativistic effects for the valence bands. The starting density—a linear superposition of free-atom densities (Ni: Ar$3d^8 4s^2$, Al: Ne$3s^2 3p$)—was calculated fully relativistically. The Kohn-Sham equations were iterated to self-consistency using a modified tetrahedron method to interpolate between **k** points in the irreducible wedge of the first Brillouin zone (IBZ).[64]

Unless otherwise stated in the text, we imposed energy cutoffs of 16 and 100 Ry (1 Ry = 13.6 eV) for the plane waves and stars, respectively, and used lattice harmonics expanded up to $l=10$ for the spherical part and $l=4$ for the nonspherical part of the MT potential. We used MT radii of 2 a.u. in all cases.

We calculated the L_3 spectra using the XSPEC routine built in to the WIEN97 software.[38] Running in absorption mode this calculates the unoccupied s and d DOS and multiplies them by their corresponding dipole matrix elements $(2p_{3/2}\rightarrow s,d)$. The treatment is very similar to that of Müller and Wilkins,[44] the only significant difference being that the integrals are carried out inside MT spheres in XSPEC, rather than the Wigner-Seitz spheres used by Müller and Wilkins. We took account of the core-hole lifetime by convolving the spectra with a Lorentzian of full width at half maximum 0.5 eV.[65]

TABLE I. Ranges and classification of the energy windows used in the calculation of the bulk charge density (see Fig. 4).

Lower bound (eV)	Upper bound (eV)	Classification
-4	-1.5	bonding
-1	1.5	nonbonding
2	4.5	antibonding

A. Bulk calculations

We used an experimentally measured lattice parameter of 5.4556 a.u. for the calculations of bulk B2 NiAl.[4] Self-consistency was assumed once all MT charges changed by less than $10^{-6}e$ on three consecutive iterations, using a **k** mesh with 84 points in the IBZ. We calculated partial DOS and L_3 edges with and without a high-lying ($E_F+22.3$ eV) Ni d local orbital as part of the basis, in order to assess the effect the linearization error had on the unoccupied partial DOS and ELNES. We evaluated the difference charge density, and the charge density within the energy windows displayed in Table I. We then increased the plane-wave and star cutoffs to 25 and 400 Ry, respectively, performed the self-consistent calculation again, and recalculated the difference charge density.

B. Grain boundary calculations

We constructed a hexagonal supercell (Space group: P6_3/mmc) containing 48 atoms and two identical $\Sigma 3$ (111) boundaries, one rotated 180 degrees about the $\overline{6}$ axis with respect to the other (see Fig. 2) to achieve periodic boundary conditions. We used fractional atomic coordinates derived from the simulation of Hagen and Finnis (courtesy of Professor M. W. Finnis) for the thirteen inequivalent z-normal planes, and the same bulk lattice parameter as in Sec. III A.

We then optimized the free internal parameters—the z coordinates of the 13 inequivalent atoms—by iterating the following procedure: (i) the internal forces were calculated self-consistently, and (ii) the z coordinates were relaxed accordingly using a damped Newton scheme.[38] Each self-consistent cycle used 16 **k** points in the IBZ. Iterative minimization was employed,[62] which provided a speed-up factor of almost three in the calculation of eigenvalues and eigenvectors, compared with diagonalizing the Hamiltonian fully. Self-consistency was assumed when the Hellman-Feynman forces on the nuclei changed by less than 0.1 mRy (a.u.)$^{-1}$ in three consecutive iterations, and then Pulay corrections to the forces were added in the final cycle.[62] We stopped the geometry minimization when the self-consistent forces on each atom dropped below 1 mRy (a.u.)$^{-1}$ We then expanded the **k**-point set to 112 points in the IBZ and repeated the self-consistent cycle once more.

We then calculated the partial DOS, ELNES, and total and difference charge densities on the $(11\overline{2}0)$ plane corresponding to mutual $\{110\}$ planes in the local, cubic coordi-

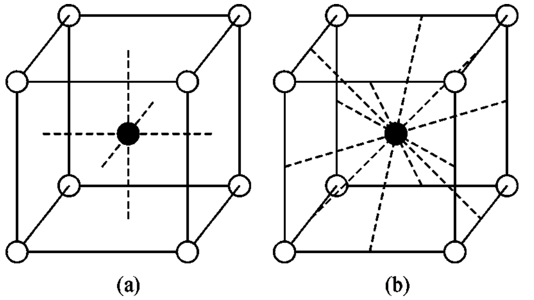

FIG. 2. Symmetry of Ni-*d* orbitals in the *B*2 structure; (a), e_g ($d_{x^2-y^2}, d_{z^2}$) and (b), t_{2g} (d_{xy}, d_{yz}, d_{zx}). Atom positions are marked; ●, Ni; ○, Al. Dashed lines show the directions along which the orbital lobes point, originating from the central Ni atom.

nate systems of the rotated crystals. Finally we simulated crude spatial difference spectra for different probe sizes,[66] weighting the contribution of each inequivalent spectrum by the number of atoms of the relevant type contained within a cylinder of a given radius, with the beam centered on the boundary and in the $[11\bar{2}0]$ direction. We carried out two calculations: one with the spectra aligned at the Fermi level, and one where we shifted each spectrum by a value equal to the self-consistent $2p_{3/2}$ core-level shift.[34]

IV. RESULTS

A. Bulk calculations

The bulk DOS, partitioned by site, and orbital angular momentum quantum number, *l* are shown in Fig. 1. Also shown are the nonequivalent e_g and t_{2g} contributions to the partial *d* DOS. For a given Ni atom, the lobes of the d-e_g orbitals point along ⟨100⟩ directions towards second-nearest-neighbor Ni atoms, and the lobes of the d-t_{2g} orbitals point along ⟨110⟩ directions towards third-nearest-neighbor Ni atoms, as shown in Fig. 2.

The calculated L_3 ELNES is shown in Fig. 3, superimposed over the unoccupied Ni *d* DOS. Including a Ni *d* local orbital in the basis boosts the overall magnitude of the unoccupied *d* DOS in an increasing fashion towards higher energies but does not significantly alter the distribution of states. The effect of the local orbital on the region of interest (0–5 eV) is negligible; thus it was considered justifiable to leave out the local orbital in the calculations that followed.

The charge density in the energy windows in Table I is plotted on the (110) and (100) planes of the unit cell in Fig. 4. The difference charge density on the (110) plane is plotted in Fig. 5 for the two different convergence criteria described in Sec. III A.

B. Grain-boundary calculations

At the start of the geometry minimization, the maximum atomic force was 12.7 m Ry $(\mathrm{a.u.})^{-1}$ acting on atom Ni12 (see Fig. 6) and the second largest 4.5 m Ry $(\mathrm{a.u.})^{-1}$ acting on atom Ni6. At the end of the minimization all forces had dropped below 1 m Ry $(\mathrm{a.u.})^{-1}$, resulting in a maximum displacement of 0.08 Å for atom Al11. All other displacements were less than half this value. All of the forces on the atoms remained below 1.1 m Ry $(\mathrm{a.u.})^{-1}$ upon expansion of the **k**-point set.

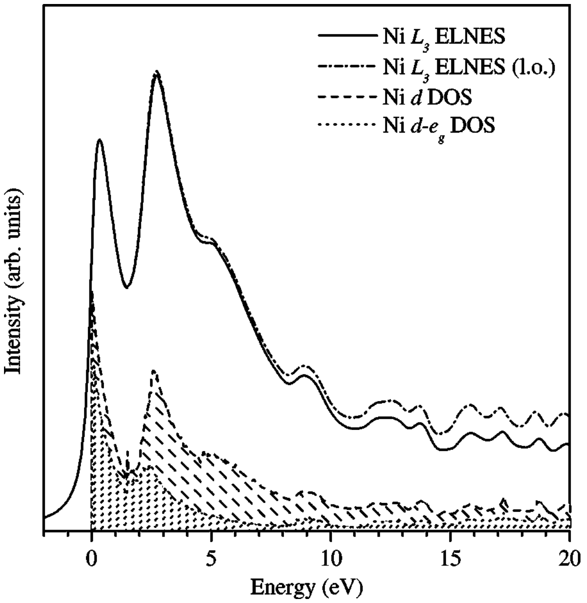

FIG. 3. Ni L_3 edges and unoccupied Ni *d* DOS calculated for bulk NiAl; (l.o.) labels the result we obtained after including a Ni *d* local orbital at 22.3 eV. The areas of the shaded regions correspond to the contribution of the e_g and t_{2g} components to the unoccupied Ni *d* DOS.

The partial Ni *d* DOS for the inequivalent Ni atoms in the supercell is shown in Fig. 7 and the corresponding L_3 edges in Fig. 8. There are large deviations from the bulk topology for the occupied *d* DOS of Ni atoms near the grain-boundary plane, which decay sufficiently rapidly that the *d* DOS for the Ni atom furthest from the grain boundary (Ni2) resembles closely that of the bulk. Similarly, the unoccupied *d* DOS and L_3 edges for the Ni atoms close to the boundary deviate significantly from the bulk calculations. Again, these deviations decay such that the bulk spectrum is well approximated for Ni2. The calculated spatial difference spectra (Fig. 9) have an oscillatory nature, going from negative to positive back to negative within the first 5 eV. The amplitude of the oscillations decays with increasing probe radius.

The difference charge density plotted on the $(11\bar{2}0)$ plane of the supercell is shown in Fig. 10. The difference charge surrounding the cores of Ni atoms close to the boundary (Ni10 and Ni12) is highly anisotropic compared to the bulk, where the deformation is approximately uniform. The difference charge density around the atoms furthest from the boundary (Al1, Ni2) approximates well that of the (110) plane of the bulk calculation.

V. DISCUSSION

A. Bulk calculations

The calculated bulk partial DOS (Fig. 1) are in good agreement with previous DFT calculations,[18,19,27,30,67] as are the calculated L_3 edges (Fig. 3).[18,19] The topology of the

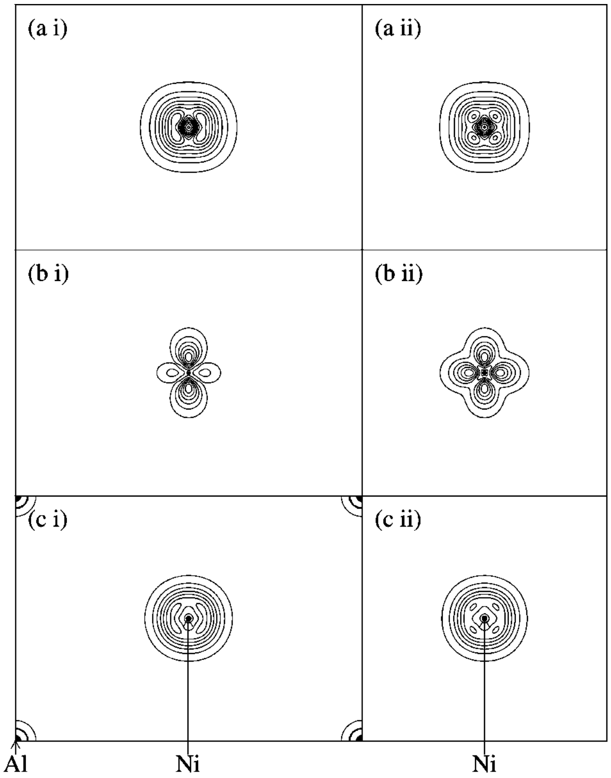

FIG. 4. Bulk charge density evaluated within the energy windows: (a) -4 to -1.5 eV (bonding states), (b) -1 to 1.5 eV (nonbonding states), (c) 2 to 4.5 eV (antibonding states); (i) on the (110) plane, (ii) on the (001) plane of the unit cell. Contours are separated by (a) 2, (b) 1, and (c) 0.25 e Å^{-3}. In-plane atom positions are labeled.

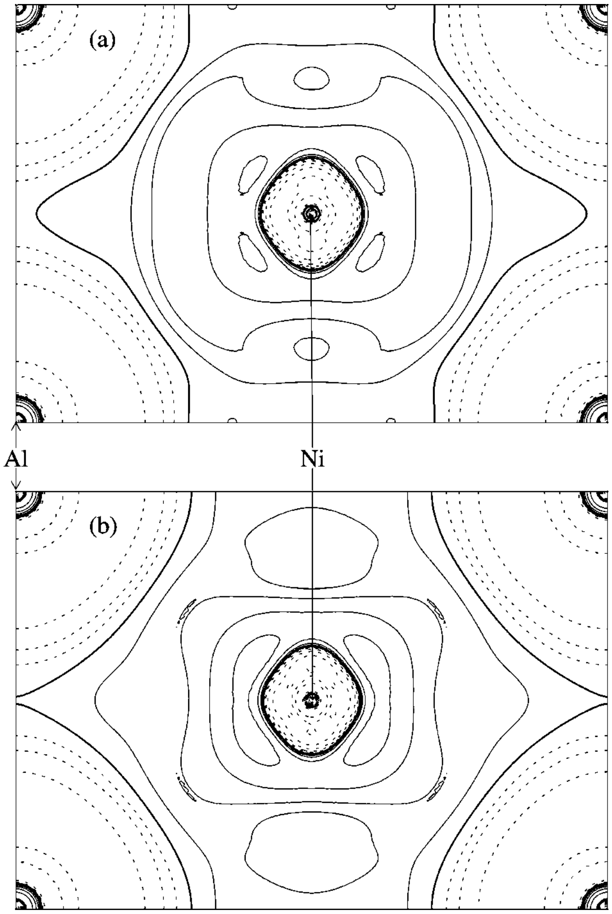

FIG. 5. Bulk difference charge density calculated on the (110) plane of the unit cell with cutoffs of (a) 16 and 100 Ry and (b) 25 and 400 Ry for the plane waves and stars, respectively. Contours are placed at $\pm 2^i/100$ e Å^{-3} ($i=0,1,2,\ldots$). Positive contours are solid; negative ones are dashed; thicker solid lines are zero contours. In-plane atom positions are labeled.

DOS, which is dominated by d states, can be understood qualitatively in terms of the model of Gelatt, *et al.*,[35] having three distinct components: bonding states (up to -1 eV), nonbonding states (-1 to 1.5 eV), and antibonding states (above 1.5 eV). There is a region of low DOS or ''pseudogap'' between the bonding and the nonbonding states, and between the nonbonding and the antibonding states, although the feature is less pronounced in the latter case. The appearance of such pseudogaps has been attributed to strong hybridization of transition-metal d with Al sp states.[31,68]

Regarding the Ni d DOS; the nonbonding orbitals have almost pure e_g ($d_{x^2-y^2}, d_{z^2}$) symmetry (Fig. 1), as pointed out by Zou and Fu,[29] but the bonding and antibonding orbitals have a mixture of t_{2g} (d_{xy}, d_{yz}, d_{zx}) and e_g symmetry (recall Fig. 2). The physical interpretation of this (see Fig. 4) is that the bonding and antibonding orbitals point from Ni towards nearest-neighbor Al atoms, whereas the nonbonding orbitals point towards second-nearest-neighbor Ni atoms. The bonding (antibonding) orbitals are pushed towards low (high) energies because of the strong hybridization with sp states of the neighboring Al atoms. Filling up the sp-d hybridized bonding orbitals thus piles up charge along the nearest-neighbor $\langle 111 \rangle$ directions, resulting in a strong Ni-Al bond, and increases the cohesive energy (in the tight-binding sense; see Ref. 69). Filling the symmetry-related antibonding states would have the opposite effect, reducing the cohesive energy.

The nonbonding states are what remains of the d-d coupling that is the predominant bonding mechanism in pure Ni, but noting that the Ni-Ni interatomic distance is 6% greater in NiAl, this second-nearest-neighbor interaction is weak

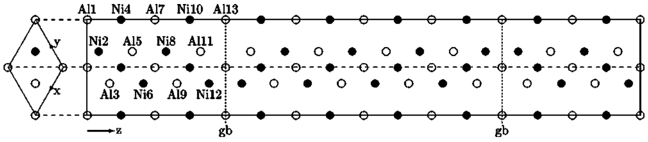

FIG. 6. Hexagonal supercell geometry used for the grain-boundary calculation. Left; projection down [0001]—in the cubic coordinate systems of the two half-crystals, (ccs1, ccs2), one of which is rotated by 180° with respect to the other, this is the [111] axis normal to the twin plane. Right: projection down $[11\bar{2}0]$ ($[1\bar{1}0]$, in ccs1; $[\bar{1}10]$, in ccs2). Atom positions are marked; ●, Ni; ○, Al. Inequivalent atom positions, grain boundaries (gb), and hexagonal axes ($x=[2\bar{1}\bar{1}0]$, $y=[\bar{1}2\bar{1}0]$, $z=[0001]$) are labeled.

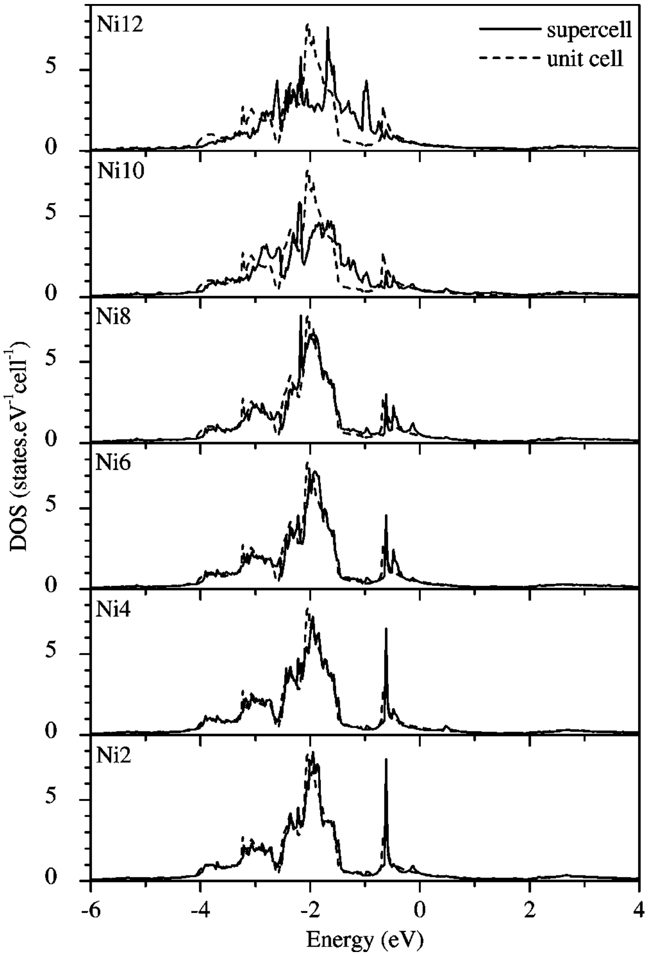

FIG. 7. Ni *d* DOS calculated for the six inequivalent Ni atoms in the supercell compared to the bulk Ni *d* DOS from the unit-cell calculation. $E_F = 0$.

in comparison to the strong, nearest-neighbor sp-d interaction.[35] Because the d-d interaction is relatively weak, these states appear in an intermediate energy range in the middle of the bonding-antibonding complex, so filling the nonbonding states does not affect the cohesive energy as greatly as filling the bonding or antibonding states. Therefore, although it may not be accurate in the strictest sense, the classification of these states as ''nonbonding'' seems reasonable in a comparative sense because the nearest-neighbor interaction is much stronger. The high stability, degree of ordering, and large heat of formation of stoichiometric NiAl[4] can hence be understood by the fact that the Fermi energy (0 eV) lies in the middle of the nonbonding states—i.e., all of the bonding states are occupied and all of the antibonding states are unoccupied.

The position of the Fermi energy in the nonbonding states also has interesting consequences for the Ni L_3 ELNES (see Fig. 3). As explained in Sec. II the Ni L_3 ELNES and the unoccupied Ni d DOS differ only by a slowly varying function of energy, so the twin-peaked fine structure just above the onset of both can be described as follows: The first peak is due to the unoccupied region of the nonbonding states, having predominantly e_g symmetry, whereas the second is due to antibonding states, which have mixed t_{2g}/e_g character similar to the bonding states. Herein lies the relationship between the Ni L_3 ELNES, the single-particle DOS, and the bonding in the material. Although ELNES samples unoccupied states, which do not participate directly in the bonding, the occupied states that do are related to them through the bonding-antibonding symmetry. This underlines the need for electronic structure calculations if the origin of the ELNES is to be properly understood.

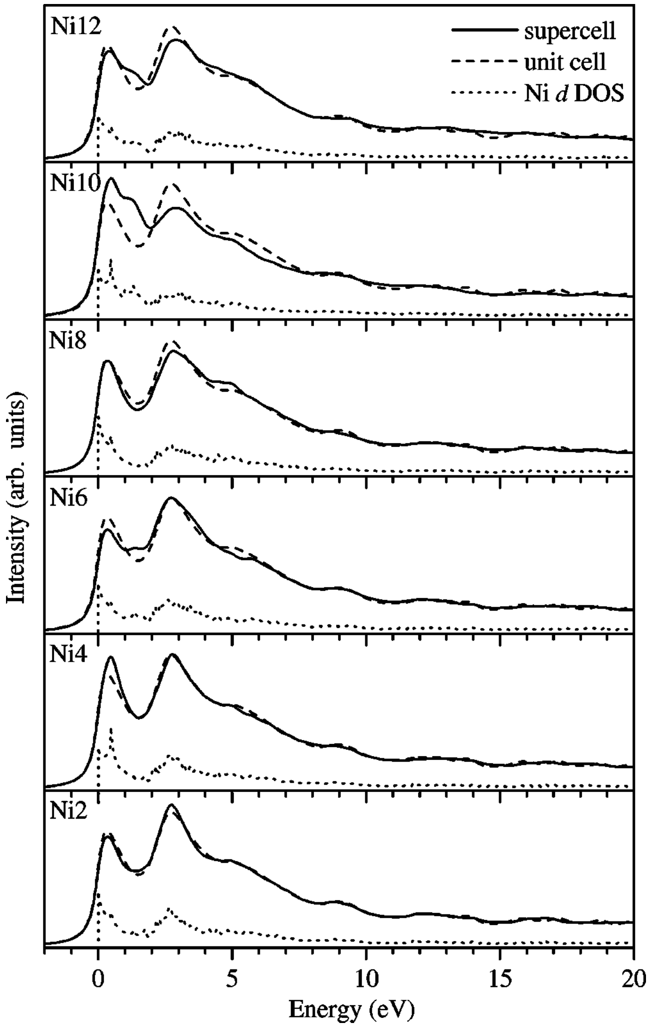

FIG. 8. L_3 edges and unoccupied *d* DOS calculated for the six inequivalent Ni atoms in the supercell, compared to the bulk Ni L_3 edges from the unit-cell calculation.

In contrast to the DOS and the Ni L_3 ELNES, the fine details of the difference charge density obtained with the lower plane-wave and star cutoffs (Fig. 5) appear somewhat crude compared with previous calculations.[25,26] Better agreement was obtained when the plane-wave and star cutoffs were increased. Note however that the features are greatly magnified in such a difference plot where the contours are not equally spaced, but separated by factors of 2. The features in the interstitial are therefore small compared to the changes near the atom cores, which are unaffected when the cutoffs are increased. It is these larger changes near the core regions to which the MT-projected partial DOS and espe-

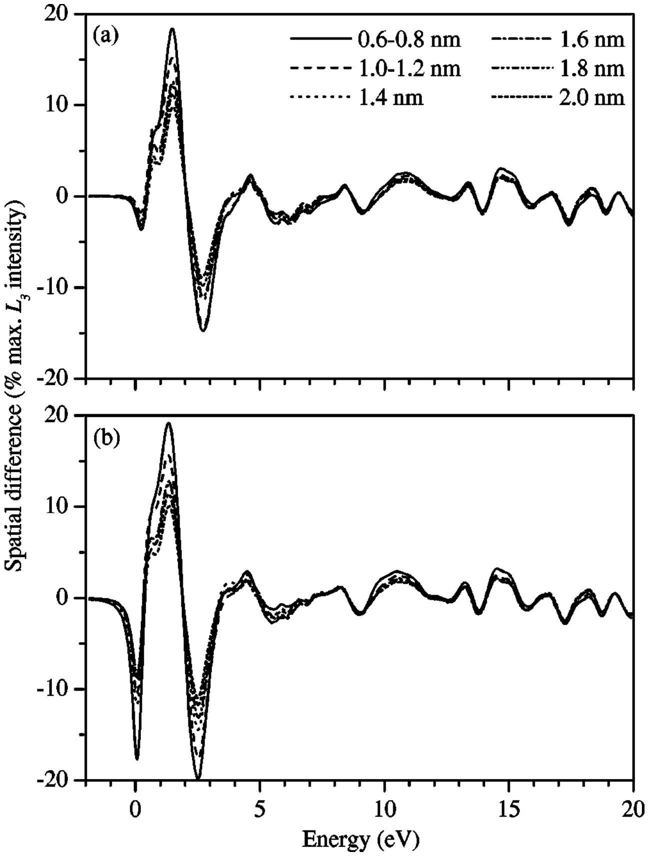

FIG. 9. Spatial difference spectra simulated for different probe diameters (see legend): (a) without, (b) including the self-consistent core-level shifts.

cially the ELNES are most sensitive. While the deformation around the Al core is approximately spherical, the region surrounding the Ni atom is noticeably aspherical, showing a preferential buildup of charge along ⟨111⟩ directions, i.e., towards nearest-neighbor Al atoms. This directionality is directly related to the strong sp-d bonding and to the inequivalence of the d-e_g and d-t_{2g} symmetries among the occupied states.

In summary, the d DOS, the Ni L_3 edges, and the difference charge density all show evidence of a crystal-field splitting of the Ni d symmetries. In other words the electronic structure has a non-negligible angular dependence. We expect therefore to see some measurable changes (via the Ni L_3 ELNES) in the electronic structure at a grain boundary where atomic relaxations and re-arrangements break the crystal-field symmetry. The angular dependence indicates further that three-body interactions need to be considered to explain the cohesive properties. Indeed Muller *et al.*,[19] have demonstrated the importance of the shape-dependent normalized fourth moment (or s parameter) of the d DOS, which to some extent takes into account this angular dependence, to explain cohesive trends in the Ni-Al system.

B. Grain-boundary calculations

The occupied Ni d DOS of the six inequivalent Ni atoms in the supercell (Fig. 7) are qualitatively similar to those calculated previously for this boundary (without *ab initio* relaxations).[39,40] The features of the d DOS of atoms Ni12 and Ni10—those nearest and second nearest the boundary plane—are considerably flattened compared with those of the bulk d DOS. In other words, states are removed from the characteristic bonding, nonbonding, and antibonding peaks, and built up in the regions between them. The intensity of the large spike located at -1.6 eV in the d DOS of atom Ni12 is greatly reduced in the present calculation, compared with the results of the previous studies. This is the most noticeable difference between the present results and those from the preliminary FLAPW calculation,[40] which used relaxed atomic coordinates from an atomistic simulation.[37] We used these as the starting coordinates for the present *ab initio* minimization, which showed little deviation from the atomistic results: The largest relaxation was 0.08 Å for Al11. It is

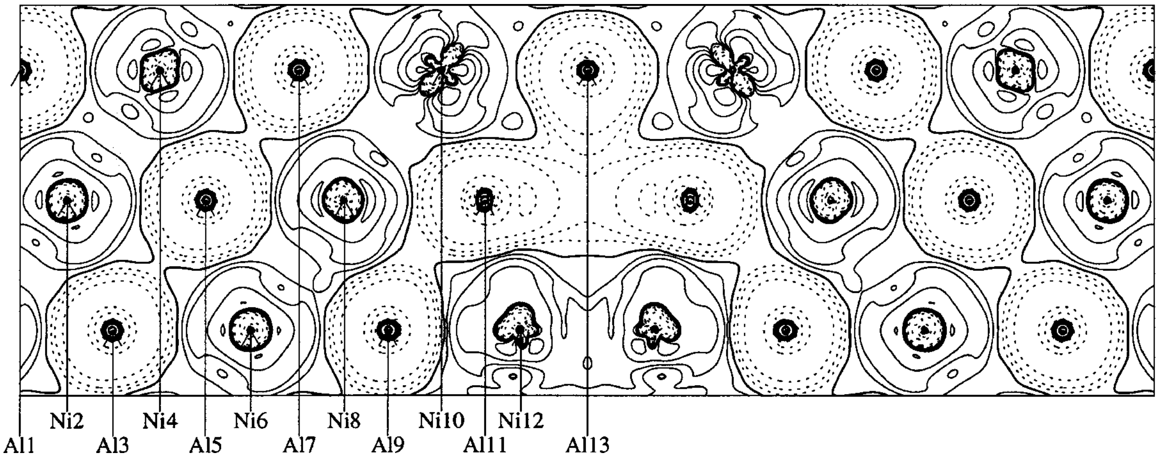

FIG. 10. Difference charge density plotted on the $(11\bar{2}0)$ plane of the supercell. Half of the supercell in the **C** direction is displayed with a grain-boundary plane at the center of the diagram, i.e., this plot covers the left-half of the right-hand side of Fig. 6. Contours are placed at $\pm 2^i/100e$ Å^{-3} ($i = 0,1,2,\dots$). Positive contours are solid; negative ones are dashed; thicker solid lines are zero contours. The inequivalent atom positions are labeled.

not surprising, therefore, that the results are very similar, and that the largest discrepancy occurs for Ni12 as mentioned above; Ni12 being adjacent to Al11, the atom for which the largest relaxation was observed.

The flattening of the features of the *d* DOS of the Ni atoms near the grain boundary can be understood as follows: The large relaxations and rearrangements break the symmetry of the crystal field that gave rise to the bonding, nonbonding, and antibonding peaks in the DOS. The e_g and t_{2g} symmetries are no longer appropriate to describe the *d* electrons, which now all experience different fields due to the relaxations, thus their individual contributions to the *d*-DOS shift and change shape by differing degrees. This has the net effect of lowering the peaks of the *d* DOS and filling in the gaps between them. This change in the shape of the *d* DOS reflects a reduction in the cohesive energy at the boundary; Muller *et al.*, identified the importance of the fourth moment of the *d* DOS in NiAl,[19] related through Aoki's bond-order expansion of the cohesive energy.[70] The *d* DOS of atom Ni2 has the roughly Lorentzian profile typical of the bulk, but approaching the boundary the *d* DOS becomes flatter and narrower, in other words more rectangular. The transition from Lorentzian to rectangular entails a reduction of the normalized fourth moment (*s*) of the *d* DOS,[69] corresponding to a reduction of the cohesive energy via Aoki's bond order expansion. The reduction of the *s* parameter results from the broken symmetry caused by the rearrangements and relaxations at the boundary, changing locally the degree of nearest-neighbor overlap and the available closed, four-step hopping paths (i.e., involving not only nearest- but also next-nearest neighbors). Simply interpreted, the shape-change shifts the center of weight of the occupied *d* DOS to higher energy, subtracting weight from the peak and tails of the Lorentzian and adding it to the gap region (around -1 eV), resulting in a less-tightly bound *d* band and hence reduced cohesive energy.

The flattening effect described above covers both the occupied and the unoccupied *d* DOS and hence is present also in the L_3 ELNES spectra (Fig. 8). Approaching the boundary, there is buildup of states in between depleted nonbonding and antibonding peaks. The results are almost identical to those obtained previously without the inclusion of *ab initio* relaxations,[40] predicting a maximum effect for Ni10, the Ni atom second closest to the grain boundary. The reason for this is not immediately obvious; we might expect the effect on Ni12 to be more extreme. However, Ni10 feels a highly distorted version of the cubic crystal field in that all of its proper nearest and next-nearest neighbors are present, whereas the crystal field around Ni12 is more complicated, involving both lattice distortions and atomic rearrangements, one of its nearest-neighbor Al atoms is replaced by Ni and three next-nearest-neighbor Ni atoms are missing. It is difficult to make a direct comparison for this reason. In any case, the important result is that the *d* DOS flattening that appeared in the bonding states is also present in the L_3 ELNES, illustrating the point that changes in the symmetry of occupied states are mirrored to some extent in the unoccupied states. Therefore, real information about bonding changes at grain boundaries can be extracted from the EEL spectrum, provided that calculations are also carried out to link changes in the occupied and unoccupied states.

The interesting features seen in the difference charge density on the $(11\bar{2}0)$ plane of the grain-boundary cell (Fig. 10) can be described as follows: (i) a deficit closely resembling the shape of a bonding $(d\text{-}t_{2g}/e_g)$ orbital at the site of atom Ni12, and (ii) a deficit with the approximate shape of a nonbonding $(d\text{-}e_g)$ orbital at the site of atom Ni10. The relaxation around Ni12 is by far the more asymmetrical of the two, re-emphasizing the point made above; Ni10 feels mainly a uniaxial distortion, whereas Ni12 feels an additional field due to the unusual coordination of the atoms surrounding it. It is clear that the directionality of the bonding increases near the boundary, a factor that may contribute to grain-boundary brittleness. However, whether or not the mechanical properties are affected, the important conclusion for this paper is that the anisotropy of the electronic structure at grain boundaries may have important consequences for the acquisition of EEL spectra. Care will have to be taken to optimize the beam convergence and spectrometer acceptance conditions in order to properly sample the different **q**'s associated with the directional final states.[51] The existence of an independent direction (z in this case) may also point towards the importance of cross terms in the DFF,[48] which are beyond the scope of this paper.

Although the present paper covers just one type of grain boundary out of the many possible low-Σ $(\Sigma \leqslant 29)$ grain boundaries in NiAl, not to mention the infinite variety of general ones, we believe the effects observed here to be largely transferable. We would expect to see similar effects at any large-angle grain boundary where distortions are required to accommodate the structure. In general this will lead to a flattening of the features of the *d* DOS, which will appear also in the L_3 ELNES.

C. Experimental outlook

The great advantage of EELS over XAS is that spectra can be acquired from very small volumes, owing to the fact that an electron beam can be focused to a fine probe. But even though it is possible in principle to obtain the 1 Å probe needed to obtain atom-column-resolved spectra in a conventional scanning transmission electron microscope (STEM), the effect of the spherical aberration (C_s) of the objective lens would limit the current density severely at such a small probe size, resulting in spectra with a poor signal-to-noise ratio. The acquisition of atom-column-resolved ELNES of a good enough quality for a comparison with the present results is probably beyond the capability of current commercial instrumentation and awaits the realization of a microscope of sufficient stability, equipped with a high-resolution spectrometer and an objective lens C_s corrector.[71] Such an instrument should be capable of delivering 100 pA into a 1 Å probe,[72] compared to 1 nA into 1 nm, typical of a C_s-uncorrected, cold field emission, dedicated 100-kV STEM.[73]

Obviously a 1-nm probe does not give atomic resolution, but nevertheless the interfacial signal may still be extracted in an averaged sense from spectra obtained with such a probe. This can be achieved using the spatial difference method,[66] where a bulk spectrum is subtracted from a spectrum taken at the grain boundary, or by multivariate statistical analysis of a spectrum-line profile crossing the grain boundary.[74] Spatial difference spectra simulated crudely from the present results (Fig. 9) show that even with a large probe (>1 nm), some interface signal may be detectable. The spatial difference spectrum has an oscillatory form corresponding to a transfer of weight from the two peaks at the onset of the Ni L_3 edge to the region between them. The inclusion of the self-consistent core-level shifts in the calculation does not alter the nature of this result. Similarly, this oscillatory signal may also be picked up as the second principal component when multivariate statistical analysis is applied to an experimental line profile. The form of the spatial difference spectrum stems from the flattening of the Ni *d* DOS discussed in Sec. V B, and indicates that even with a 1nm probe it may be possible to detect changes in the bonding that can be related to changes in cohesion at an NiAl grain boundary. Indeed this statement applies to any ordered material where a crystal-field effect is present in the $L_{2,3}$ ELNES.

It will be important while performing the experiments to differentiate between the effects described above and those due to segregation of impurities, grain-boundary nonstoichiometry, and specimen and surface oxide thickness variations. These may affect the measured ELNES severely leading to an erroneous interpretation, but can be monitored to a great extent by carefully analyzing the whole EEL spectrum and taking complementary x-ray energy dispersive spectra. Also, they will lead in general to a nonzero net contribution to the spatial difference spectrum, whereas an integration of the calculated spectrum in Fig. 9 predicts zero net spatial difference. Another effect that must be monitored is that of electron-beam-induced specimen damaging; the exit-surface sputtering caused by the intense probe of a dedicated STEM is particularly severe for the clean specimens we wish to examine. It has been shown that this process can be slowed dramatically by coating the specimen with a thin carbon film.[75] With these considerations in mind, experiments are planned involving the acquisition of Ni $L_{2,3}$ spectra from a bicrystalline specimen of stoichiometric NiAl containing the same $\Sigma 3$ (111) boundary studied here.

VI. CONCLUSION

We have shown using one-electron band-structure calculations how the crystal field set up by the sp-d hybridization influences the Ni L_3 electron ELNES in NiAl. We have predicted that as a consequence the Ni L_3 ELNES should be sensitive to the type of lattice distortions and atomic rearrangements that occur at grain boundaries. Our supercell calculations involving a $\Sigma 3$ (111) grain boundary bear out this assertion, predicting a flattening of the partial density of Ni *d* states that can be detected also in the calculated Ni L_3 ELNES. The flattening of the spectral features can be linked to a change in shape of the density of Ni *d* states from a Lorentzian to a more rectangular profile, shifting the center of weight of the *d* band higher in energy and lowering the cohesive energy of atoms at the grain boundary. We have predicted that the small changes observed in the calculated spectra should be measurable using not only an instrument capable of forming an atomic-sized probe, but also using a larger probe on a conventional cold-field-emission analytical electron microscope.

ACKNOWLEDGMENTS

We thank Professor M. W. Finnis for providing the atomic coordinates used for the starting geometry in this work, and thank also A. Scott and W. M. Temmerman for useful discussions. The work was carried out on an EPSRC studentship with additional funding from the Foresight Challenge Project.

---

*Corresponding author. Electronic address: dap31@cam.ac.uk

[1] P. E. Batson, Nature (London) **366**, 727 (1993).

[2] P. E. Batson, Ultramicroscopy **78**, 33 (1999).

[3] D. A. Muller, T. Sorsch, S. Moccio, F. H. Baumann, K. Evans-Lutterodt, and G. Timp, Nature (London) **399**, 758 (1999).

[4] R. D. Noebe, R. R. Bowman, and M. V. Nathal, Int. Mater. Rev. **38**, 193 (1993).

[5] D. B. Miracle, Acta Metall. Mater. **41**, 649 (1993).

[6] R. Darolia, J. Inst. Met. **43**, 44 (1991).

[7] A. Wenger, G. Bürri, and S. Steinemann, Solid State Commun. **9**, 1125 (1971).

[8] W. Blau, J. Weisbach, G. Merz, and K. Kleinstück, Phys. Status Solidi B **93**, 713 (1979).

[9] S. B. Maslenkov, A. I. Kozlenkov, S. A. Filin, and A. I. Shuglin, Phys. Status Solidi B **123**, 605 (1984).

[10] P. O. Nilsson, Phys. Status Solidi **41**, 317 (1970).

[11] S. P. Kowalczyk, G. Apai, G. Kaindl, F. R. McFeely, L. Ley, and D. A. Shirley, Solid State Commun. **25**, 847 (1978).

[12] J. C. Fuggle, F. U. Hillebrecht, R. Zeller, Z. Zołnierek, P. A. Bennet, and C. Freiburg, Phys. Rev. B **27**, 2145 (1983).

[13] F. U. Hillebrecht, J. C. Fuggle, P. A. Bennet, Z. Zołnierek, and C. Freiburg, Phys. Rev. B **27**, 2179 (1983).

[14] D. D. Sarma, W. Speier, R. Zeller, E. van Leuken, R. A. de Groot, and J. C. Fuggle, J. Phys.: Condens. Matter **1**, 9131 (1989).

[15] S. C. Lui, J. W. Davenport, E. W. Plummer, D. M. Zehner, and G. W. Fernando, Phys. Rev. B **42**, 1582 (1990).

[16] D. M. Pease and L. V. Azároff, J. Appl. Phys. **50**, 6605 (1979).

[17] T. K. Sham, Solid State Commun. **64**, 1103 (1987).

[18] G. A. Botton, G. Y. Guo, W. M. Temmerman, and C. J. Humphreys, Phys. Rev. B **54**, 1682 (1996).

[19] D. A. Muller, D. J. Singh, and J. Silcox, Phys. Rev. B **57**, 8181 (1998).

[20] V. L. Moruzzi, A. R. Williams, and J. F. Janak, Phys. Rev. B **10**, 4856 (1974).

[21] C. Müller, H. Wonn, W. Blau, P. Ziesche, and V. P. Krivitskii, Phys. Status Solidi B **95**, 215 (1979).

[22] D. Hackenbracht and J. Kübler, J. Phys. F: Met. Phys. **10**, 427 (1980).

[23] K. Pechter, P. Rastl, A. Neckel, R. Eibler, and K. Schwarz,

Monatsch. Chem. **112**, 317 (1981).

[24] C. Müller, W. Blau, and P. Ziesche, Phys. Status Solidi B **116**, 561 (1983).

[25] C. L. Fu and M. H. Yoo, Acta Metall. Mater. **40**, 703 (1992).

[26] Z. W. Lu, S.-H. Wei, and A. Zunger, Acta Metall. Mater. **40**, 2155 (1992).

[27] O. V. Farberovich, S. V. Vlaslov, K. I. Portnoi, and A. Y. Lozovoi, Physica B **182**, 267 (1992).

[28] P. A. Schultz and J. W. Davenport, J. Alloys Compd. **197**, 229 (1993).

[29] J. Zou and C. L. Fu, Phys Phys. Rev. B **51**, 2115 (1995).

[30] V. Sundarajan, B. R. Sahu, D. G. Kanhere, P. V. Panat, and G. P. Das, J. Phys.: Condens. Matter **7**, 6019 (1995).

[31] D. Nguyen Manh, D. Mayou, A. Pasturel, and F. Cyrot-Lackmann, J. Phys. F: Met. Phys. **15**, 1911 (1985).

[32] A. Pasturel and P. Hichter, J. Less-Common Met. **86**, 181 (1982).

[33] C. Colinet, A. Bessoud, and A. Pasturel, J. Phys.: Condens. Matter **1**, 5837 (1989).

[34] D. A. Muller, P. E. Batson, and J. Silcox, Phys. Rev. B **58**, 11 970 (1998).

[35] C. D. Gelatt, Jr., A. R. Williams, and V. L. Moruzzi, Phys. Rev. B **27**, 2005 (1983).

[36] K. Nadarzinsky and F. Ernst, Mater. Sci. Forum **207-209**, 309 (1996).

[37] M. Hagen and M. W. Finnis, Mater. Sci. Forum **207-209**, 245 (1996).

[38] P. Blaha, K. Schwarz, and J. Luitz, in WIEN97, *A Full Potential Linearized Augmented Plane Wave Package for Calculating Crystal Properties*, edited by Karlheinz Schwarz (Technical Universität Wien, Austria., 1999), ISBN 3-9501031-0-4.

[39] D. A. Pankhurst, G. A. Botton, and C. J. Humphreys, in *Electron Microscopy 1998*, edited by H. A. C. Benavides and M. J. Yacaḿan (Institute of Physics, Bristol, 1998), Vol. Y.II, pp. 643–644.

[40] D. A. Pankhurst, G. A. Botton, and C. J. Humphreys, in *Electron Microscopy and Analysis 1999*, Vol. 161 of Institute of Physics Conference Series, edited by C. J. Kiely (Institute of Physics, Bristol, 1999), pp. 67–70.

[41] H. Bethe, Ann. Phys. (Leipzig) **5**, 325 (1930).

[42] M. Inokuti, Rev. Mod. Phys. **43**, 297 (1971).

[43] H. A. Bethe and E. E. Salpeter, in *Quantum Mechanics of One- and Two-Electron Atoms* (Springer-Verlag, Berlin, 1957), Chap. 4.

[44] J. E. Müller and J. W. Wilkins, Phys. Rev. B **29**, 4331 (1984).

[45] J. C. Slater, Phys. Rev. **51**, 846 (1937).

[46] D. A. Goodings and R. Harris, J. Phys. C **2**, 1808 (1969).

[47] A. Neckel, K. Schwarz, R. Eibler, P. Rastl, and P. Weinberger, Mikrochim. Acta **6**, 17 (1975).

[48] M. Nelhiebel, P.-H. Louf, P. Schattschneider, P. Blaha, K. Schwarz, and B. Jouffrey, Phys. Rev. B **59**, 12 807 (1999).

[49] C. Hébert-Souche, P.-H. Louf, P. Blaha, M. Nelhiebel, J. Luitz, P. Schattschneider, K. Schwarz, and B. Jouffrey, Ultramicroscopy **83**, 9 (2000).

[50] R. F. Egerton, *Electron Energy-Loss Spectroscopy in the Electron Microscope*, 2nd ed. (Plenum, New York, 1996).

[51] N. K. Menon and J. Yuan, Ultramicroscopy **74**, 83 (1998).

[52] L. J. Sham and W. Kohn, Phys. Rev. B **145**, 561 (1966).

[53] P. Lerch, T. Jarlborg, V. Codazzi, G. Loupias, and A. M. Flank, Phys. Rev. B **45**, 11 481 (1992).

[54] S. Köstlmeier and C. Elsässer, Phys. Rev. B **60**, 14 025 (1999).

[55] E. A. Stern and J. J. Rehr, Phys. Rev. B **27**, 3351 (1983).

[56] L. Hedin and S. Lundqvist, in *Solid State Physics*, edited by F. Seitz, D. Turnbull, and H. Ehrenreich (Academic, New York, 1969), Vol. 23, pp. 1–181.

[57] R. W. Godby, M. Schlüter, and L. J. Sham, Phys. Rev. B **37**, 10 159 (1988).

[58] P. Horsch, W. von der Linden, and W.-D. Lukas, Solid State Commun. **62**, 359 (1987).

[59] W. Speier, R. Zeller, and J. C. Fuggle, Phys. Rev. B **32**, 3597 (1985).

[60] J. R. Willhite, L. B. Welsh, T. Yoshitomi, and J. O. Brittain, Solid State Commun. **13**, 1907 (1973).

[61] N. I. Kulikov, A. V. Postnikov, G. Borstel, and J. Braun, Phys. Rev. B **59**, 6824 (1999).

[62] D. J. Singh, *Planewaves, Pseudopotentials and the LAPW Method* (Kluwer, Boston, 1994).

[63] J. P. Perdew and Y. Wang, Phys. Rev. B **45**, 13 244 (1992).

[64] P. E. Blöchl, O. Jepsen, and O. K. Andersen, Phys. Rev. B **49**, 16 223 (1994).

[65] M. O. Krause and J. H. Oliver, J. Phys. Chem. Ref. Data **8**, 329 (1979).

[66] H. Müllejans and J. Bruley, Ultramicroscopy **53**, 351 (1994).

[67] D. J. Singh, in *Intermetallic Compounds: Principles and Practice*, edited by J. H. Westbrook and R. L. Fleischer (Wiley, New York, 1994), Vol. 1, pp. 127–147.

[68] G. Trambly de Laissardiére, D. Nguyen Manh, L. Magaud, J. P. Julien, F. Cyrot-Lackmann, and D. Mayou, Phys. Rev. B **52**, 7920 (1995).

[69] A. P. Sutton, *Electronic Structure of Materials* (Oxford, Oxford, 1993).

[70] M. Aoki, Phys. Rev. Lett. **71**, 3842 (1993).

[71] O. L. Krivanek, N. Dellby, and A. R. Lupini, Ultramicroscopy **78**, 1 (1999).

[72] A. R. Lupini (private communication).

[73] L. M. Brown, in *Impact of Electron and Scanning Probe Microscopy on Materials Science*, Vol. 364 of NATO Sciences Series E: Applied Science, edited by D. G. Rickerby, G. Valdré, and U. Valdré (Kluwer, Dordrecht, The Netherlands, 1999), pp. 209–230.

[74] N. Bonnet, N. Brun, and C. Colliex, Ultramicroscopy **77**, 97 (1999).

[75] D. A. Muller and J. Silcox, Philos. Mag. A **71**, 1375 (1995).